One-Pot Synthesis of Binderless Zeolite a Spheres via *In Situ* Hydrothermal Conversion of Silica Gel Precursors

Hui Sun, Zhongwei Sun, Benxian Shen, and Jichang Liu
School of Chemical Engineering, Petroleum Processing Research Center, East China University of Science and Technology, Shanghai 200237, China

State Key Laboratory of Chemical Engineering, East China University of Science and Technology, Shanghai 200237, China

Gengnan Li
The Gene and Linda Voiland School of Chemical Engineering and Bioengineering, Washington State University, Pullman, WA 99163

Di Wu
The Gene and Linda Voiland School of Chemical Engineering and Bioengineering, Washington State University, Pullman, WA 99163

Dept. of Chemistry, Washington State University, Pullman, WA 99163

Dept. of Materials Science and Engineering, Washington State University, Pullman, WA 99163

Yuxin Zhang
School of Chemical Engineering, Petroleum Processing Research Center, East China University of Science and Technology, Shanghai 200237, China

DOI 10.1002/aic.16200
Published onlineJuly 24, 2018 in Wiley Online Library (wileyonlinelibrary.com)

One-pot synthesis route was explored for preparing binderless zeolite A via an in situ hydrothermal transformation process involving the preformation of silica gel precursors. Synthesis process was optimized and resulting samples were characterized using XRD, Raman spectroscopy, EDS, ^{29}Si and ^{27}Al NMR spectroscopy, SEM, HRTEM, and pore structure analyses. Furthermore, the kinetics for the in situ synthesis was investigated and the underlying crystallization mechanism was interpreted. The transformation of silica precursors was accomplished via controlling the synthesis parameters which govern the crystallization through determining the dissolution rate of silica nanoparticles, diffusion of Al species into silica precursors and crystal nuclei growth. Subsequently, Al species could contact and react with released Si species from silica nanoparticles to build the structural units that finally construct the LTA framework through self-organized arrangement. On pure zeolite A phase basis, the synthesized binderless sample exhibits higher specific surface area and n-paraffins adsorption capacity than binder-containing zeolite. © 2018 American Institute of Chemical Engineers *AIChE J* 64: 4027–4038 2018

Keywords: binderless zeolite A, in situ hydrothermal synthesis, crystallization kinetics, mechanism

Introduction

Due to their enormous applications in various industrial processes including adsorption and separation, ion exchange, shape selective catalysis, sensing and medical treatment, aluminosilicate zeolites have received wide attention from both scientific and engineering societies.[1–8] Hydrothermal conversion is the most extensively used method in the synthesis of zeolites[9,10] that are conventionally produced in the form of powder. Binders, such as clay, kaolin or silica sol, are added into zeolite powders to form monoliths and achieve satisfactory mechanical strength for practical applications.[11,12] However, the addition of binder has a variety of undesirable influences on adsorption,[13–15] diffusion,[16] and coking deactivation.[17,18] Moreover, the inorganic binders can largely affect the catalytic activity of zeolite-derived catalysts.[19,20] Therefore, a large number of studies have been done on preparing shape-controlled zeolites avoiding the use of inorganic binders. A preparation process of binderless zeolites A was proposed by Universal Oil Products Company (UOP) as early as 1960s.[21,22] The silica granules were first preformed in a hot oil-ammonia solution system and thereafter converted into

Additional Supporting Information may be found in the online version of this article.

Correspondence concerning this article should be addressed to H. Sun at sunhui@ecust.edu.cn.

Table 1. Several Providers of Commercial Binderless Zeolite 5A

Provider	Country	Product Series
Chemiewerk Bad Köstritz GmbH	Germany	KÖSTROLITH® 5ABF
Grace Davison	USA	SYLOBEAD® S624
Tosoh	Japan	ZEOLUM® SA-500
Nanjing Petrochemical Refinery Co., Ltd	China	NWA-II
Yandan Chemical Co., Ltd	China	Binderless CaA

zeolite A in a hydrothermal sodium aluminate solution. Improved techniques were reported by the following researchers.[23] Table 1 lists several providers of commercial binderless zeolites. However, such methods involved hot ammonia as well as kerosene as the media, therefore, gave rise to the environmental problems. Extensive investigations have been performed to achieve a series of performance-enhanced zeolites, including ZSM-5,[24] P,[25] X,[16] Y,[15] silicalite-1,[26] and zeolite tubes.[27] Different methods, such as dry-gel conversion,[28] solvent-free route,[29,30] binder transformation[31] using preformed extrudes, direct conversion of glass materials,[32] and the pseudomorphic transformation technique[15,33] were developed and employed successfully. However, existing methods for the synthesis of binderless zeolite particles usually concern multistep procedures including the preparation of composite precursors (e.g., silica, alumina, natural, or synthetic aluminosilicates) and subsequent hydrothermal conversion of these precursors in various alkaline systems. Recently, the bioorganic molecule—assisted three-step (impregnation—gelation—hydrothermal synthesis) method was explored and used in the synthesis of hybrid zeolite microspheres.[34,35] After removing the organic components by calcination, binderless zeolite architectures could be achieved. Both route-shortening and step-reducing can benefit to reduce the time and capital consumption during the binderless zeolite production. Moreover, understanding the underlying mechanism and kinetics for the in situ construction of zeolite A framework structure from preformed composite precursors is realized to be of significant implications for the controllable preparation of function-strengthened porous materials.

In this article, we reported the synthesis of granular binderless zeolite A via in situ hydrothermal transformation of silica gel precursors. By replacing the NaOH aqueous solution or ammonia with sodium aluminate alkaline solution during the preparation of silica gel precursors using silica sol as Si source, the synthesis could be accomplished through one-pot process. The synthesized product exhibits characteristic morphology and high purity of crystalline phase of zeolite A and significantly higher adsorption ability as compared with the binder-containing sample. In addition, present study provides the insight into the crystallization kinetics and mechanism for the in-situ conversion from silica precursors to zeolite spheres.

Experimental

Materials

Sodium metaaluminate (98.5% purity) and cetyltrimethyl ammonium bromide (CTAB) (99% purity) were obtained from Aladdin Industrial reagent corporation (Shanghai, China). Normal paraffins (98.5% purity), calcium chloride (98.5% purity) were provided by Shanghai Lingfeng Chemical Reagent Co., Ltd (Shanghai, China). Sodium hydroxide (96.0% purity) and ammonium chloride (99.5% purity) were purchased from Sinopharm Chemical Reagent Co., Ltd (Shanghai, China). Silica sol (solid content of 40 wt % and average particle size of 50 nm) was offered by Qingdao Fuso Refining & Processing Co., Ltd (Qingdao, China). The binder-containing zeolite 5A obtained from Honeywell International Inc. (Shanghai, China) was used as a reference sample and its chemical composition on the basis of oxide is shown in Supporting Information Table S1. Furthermore, the mass fraction of binder contained in the reference sample is evaluated to be 19.2% according to the result of X-ray diffraction[36] (see Supporting Information Figure S1). A commercial binder-free 5A sample provided by Yandan Chemical Co., Ltd (Zhangzhou, China) was also used as reference. All of the chemicals were used as received without further purification.

One-pot synthesis of granular binderless zeolite A

A custom-made oil/water two phase column using 30 mL heptane as oil phase, 235 mL sodium aluminate alkaline solution (dissolving 49.2 g sodium metaaluminate and 4∼24 g sodium hydroxide into 216 g deionized water) as water phase, and saturated CTAB aqueous solution in the oil/water interface was prepared in a beaker for preforming the silica gel precursors (see Figure 1 for the schematic diagram). First, the silicon source was prepared by adding 9 mL ammonium chloride solution (with mass fraction of 10%) into 45 g aforementioned silica sol solution under magnetically stirring. Then the resulting silica sol mixture was dropped dropwise into the two-phase column from the top (upper oil phase). The silica sol droplets could keep morphology of sphere when they were introduced into oil phase because of the oil/water interface tension. The saturated CTAB aqueous solution was used as surfactant for helping the silica sol droplets to cross the oil/water interface more easily, then solidify into silica gel spheres (having a diameter of 3∼4 mm) in the alkaline solution phase and settle at the bottom of the beaker. The amount of silica sol droplets introduced into the beaker was well controlled to reach a certain chemical composition of the hydrothermal synthesis system (molar composition of 3 SiO_2: 6 $NaAlO_2$: (1∼6) NaOH: 120 H_2O). Then the bottom alkaline solution together with formed silica gel spheres was separated and transferred into a sealable autoclave with Teflon inner. The hydrothermal reaction was performed in the autoclave and kept at different temperatures (ranging from 60 to 100°C) for 0 to 48 h. Subsequently, the resulting products were separated from the synthesis mother liquor by filtration and washed with deionized water until the pH value of the washing water reached about 9. The collected samples were finally dried at 90°C overnight.

Calcium ion exchange

Calcium ion exchange was implemented to transform the synthesized zeolite A from type Na into type Ca to endow it with selective adsorption affinity to normal paraffins from hydrocarbon mixtures. Ca-exchange was performed at 80°C for 6 h by immersing 20 g synthesized binderless zeolite NaA spheres into 200 mL $CaCl_2$ aqueous solution (0.5 M) with stirring the upper liquid using a mechanical agitator. The resulting solid products were successively separated by filtration, washed with deionized water for three times, dried at 90°C overnight, and kept in desiccator remaining a constant relative humidity prior to further characterization.

Characterization

X-ray diffraction (XRD) analyses were performed at room temperature using a D/Max 2550 X-ray diffractometer

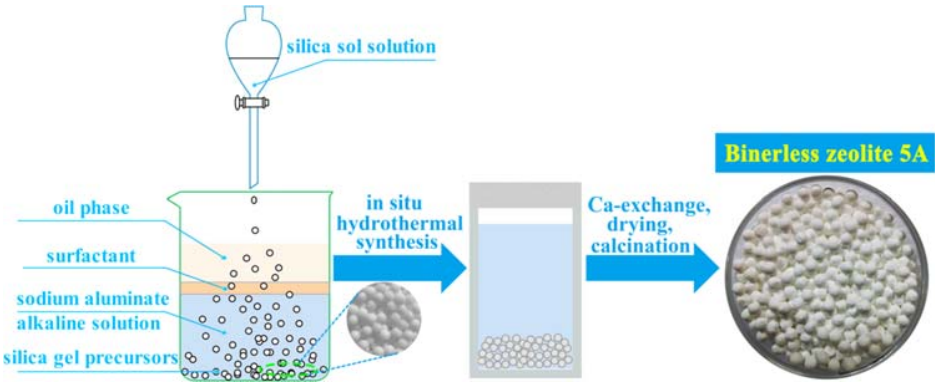

Figure 1. Schematic diagram for one-pot synthesis of binderless zeolite A granules.

[Color figure can be viewed at wileyonlinelibrary.com]

operated at 40 kV and 100 mA with Cu Kα radiation. Data were collected from 5 to 60°. All the XRD patterns were refined using Jade 6.0 and ICSD database and then the phase compositions were determined.

The crystal morphology of synthesized zeolite A was obtained using a Philips XL 30 scanning electron microscope (SEM) operated at 5 kV. Elemental analyses were performed on a Falcon energy-dispersive spectrometer (EDS) (EDAX Inc.). Five to eight points were measured at various positions to obtain an average elemental composition. Homogeneity was checked using backscattered electron (BSE) imaging. The relative average deviation is around ±5%.

High-resolution transmission electron microscopy (HRTEM) analyses were carried out at a JEOL JEM-2100 electron microscope. The samples were dispersed in absolute ethanol with an ultrasonic bath, and then obtained suspension was dropped onto copper TEM grids coated with a holey carbon film.

Raman spectra were measured with a LabRAM HR800 spectrometer fitted with a 325 nm laser. Data were recorded from 1200 to 200 cm^{-1} with a spectral resolution of 1.6 cm^{-1}.

Pore structures of different zeolite 5A samples were determined by N_2 adsorption at 77 K using a 3H-2000PM2 automatic physisorption analyzer (BeiShiDe Instrument Co., Ltd., Beijing, China). Specific surface areas were calculated using the Brunauer−Emmett−Teller (BET) method. Micropore and mesopore volumes were calculated using the Harvath−Kawazoe (H-K) method and Barrett-Joyner-Halenda (BJH) method, respectively. Pore volumes and pore size distributions of macropore were determined by employing an Auto Pore IV 9510 mercury injection apparatus (Micromeritics, Norcross GA). Adsorption isotherms of normal paraffins on different zeolite 5A samples were determined at 298 K using a 3H-2000PW gravimetric vapor adsorption analyzer (BeiShiDe Instrument Co., Ltd., Beijing, China). All samples were degassed at 300°C for 12 h prior to measurements.

Solid-state ^{29}Si and ^{27}Al magic angle spinning (MAS) NMR spectra were acquired using a Bruker AVANCE-III 500 MHz spectrometer (Bruker, Germany) equipped with a 4 mm MAS probe. The ^{29}Si and ^{27}Al chemical shifts were referenced to tetramethylsilane (0 ppm) and 1 M $AlCl_3$ aqueous solution (0 ppm), respectively.

Mechanical properties of samples were tested by employing a KQ-3 compressive strength measuring device (Kehuan Analysis Technology Limited Co., Ltd, China). Mechanical strength measurement for each sample was repeated at least 20 times to obtain an average value.

Results and Discussion

Effect of crystallization time

The granular silica gel precursors formed in the sodium aluminate solution were in situ converted under 80°C. Figure 2A

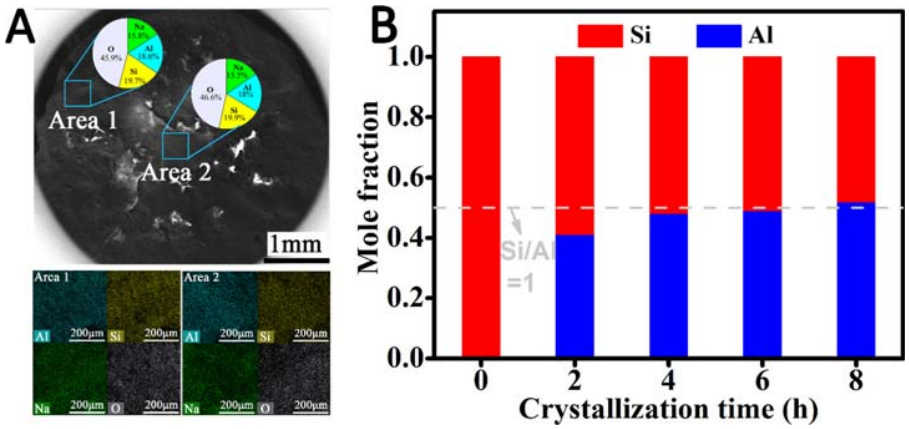

Figure 2. (A) EDS mapping analyses on the sample synthesized under 80°C for 6 h. (B) Relative contents of Al and Si for the synthesized samples using NaOH concentration of 1.6 mol/L, crystallization temperature of 80°C, and crystallization times increasing from 0 to 8 h.

[Color figure can be viewed at wileyonlinelibrary.com]

Table 2. Chemical Compositions (on TO_2 Basis), Lattice Parameters and Relative Crystallinities for Different Samples Synthesized under Various Conditions

Sample No.	Crystallization Time [h]	Crystallization Temperature [°C]	*c*(NaOH) [mol/L]	Chemical Composition	Lattice Parameter	Relative Crystallinity [%]
S1	0	80	1.6	SiO_2	0	0
S2	2	80	1.6	$Na_{0.412}Al_{0.412}Si_{0.588}O_2$	24.1476	47.8
S3	4	80	1.6	$Na_{0.483}Al_{0.483}Si_{0.517}O_2$	24.2193	92.5
S4	6	80	1.6	$Na_{0.489}Al_{0.489}Si_{0.511}O_2$	24.3451	99.4
S5	8	80	1.6	$Na_{0.520}Al_{0.520}Si_{0.480}O_2$	24.6204	99.5
S6	6	60	1.6	$Na_{0.332}Al_{0.332}Si_{0.668}O_2$	24.1838	42.5
S7	6	70	1.6	$Na_{0.477}Al_{0.477}Si_{0.523}O_2$	24.5507	85.7
S8	6	90	1.6	$Na_{0.489}Al_{0.489}Si_{0.511}O_2$	24.4434	97.6
S9	6	100	1.6	$Na_{0.509}Al_{0.509}Si_{0.491}O_2$	24.0805	90.9
S10	6	80	0.8	$Na_{0.482}Al_{0.482}Si_{0.518}O_2$	24.6672	81.4
S11	6	80	1.2	$Na_{0.487}Al_{0.487}Si_{0.513}O_2$	24.5955	93.9
S12	6	80	2.0	$Na_{0.493}Al_{0.493}Si_{0.507}O_2$	24.5775	94.7
S13	6	80	2.4	$Na_{0.487}Al_{0.487}Si_{0.513}O_2$	24.5180	93.3

shows the elemental compositions obtained from EDS mapping analysis on as-synthesized sample S4 (see Table 2) undergoing 6 h of crystallization time. The consistent Al contents in two distinct areas (18.6% for area 1 and 18.0% for area 2, in mass basis) suggest the well-defined composition of the in situ converted product. With the increase of crystallization time, Al species in the bulk solution gradually diffuse into the spherical silica precursors and induce a composition evolution to zeolite A phase. As a result, the Al/Si molar ratios initially increase and reach a plateau at approximately 1.0 (see Figure 2B and Table 2), which is that of ideal zeolite A framework.

The powder XRD patterns for synthesized samples at different crystallization times are presented in Figure 3. From the XRD results, the initially formed silica precursors are observed completely amorphous phase (see sample S1 in Figure 3). After 2 h, the sample S2 exhibits characteristic diffraction peaks corresponding to zeolite A framework at 7.17°, 10.15°, 12.46°, 16.11°, 21.67°, 23.99°, 27.13°, 29.96°, and 34.20°, and a very similar lattice parameter *a* of 24.1476 compared with the documented value.[37] In addition, its relative crystallinity is of 47.8%, indicating an initial crystallization (sample having low Al content from Figure 2B). As the crystallization time is increased to 4 h, the product exhibits a high purity of zeolite A phase by giving a largely enhanced crystallinity of 92.5%. Further increase in crystallization time exerts slight effect on the crystal phase transition. The sample displays higher relative crystallinity of 99.4% and larger *a* of 24.3451 at 6 h (see Table 2). To further understand the in situ synthesis process, the morphology analyses of the samples collected at different times were performed and the SEM and TEM images are presented in Figures 4 and 5, respectively. The initial silica precursors (the sample S1) exhibit as the aggregates of spherical silica nanoparticles with a size of around 50 nm. There are no Al species involved in the preformed precursors (see Figure 2B for the Al content of 0 h sample). Two hours later, some semicrystallized particles are observed at the core of the aggregates and surrounded by the silica nanoparticles that have not taken part in the zeolitic framework construction. From the SEM and TEM images of the 4 h sample, silica nanoparticles disappear completely and the cubic crystals of zeolite A can be clearly recognized to interlace with each others. The samples undergoing 6 and 8 h of crystallization time display the very similar crystal morphologies, which agree well with the XRD analysis results.

Effect of crystallization temperature

To examine the effect of temperature on crystallization, the in situ conversion was performed at different temperatures varying from 60 to 100°C for a fixed reaction time of 6 h (see Figures 6 and 7 for XRD patterns and SEM images). The results indicate that the relative crystallinity of zeolite A phase initially increases with the temperature and reaches a plateau of 99.4% at 80°C (see Figure 6). In addition, the SEM measurements (see Figure 7) clearly display the crystallization process: the formation of zeolite A structures accompanies with the consumption of silica nanoparticles. Continuing to increase the crystallization temperature up to 100°C, an additional weak diffraction peak appears at 13.94° corresponding to sodalite (SOD), resulting from the LTA-to-SOD phase transition. SEM image for 100°C sample also demonstrates the evolution of crystal morphologies. The same phase transition has been observed in the conventional hydrothermal synthesis of zeolite A when using high crystallization temperatures or prolonged conversion time.[38] As for the in situ conversion initiated from silica precursors, the crystallization temperature can not only partially determine the rates of nucleation and

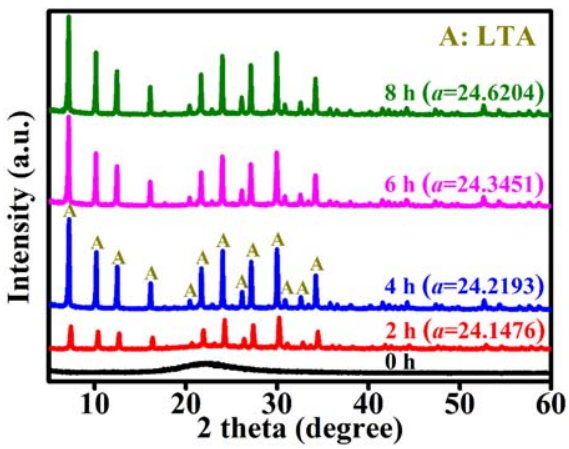

Figure 3. XRD patterns of synthesized samples using NaOH concentration of 1.6 mol/L, crystallization temperature of 80°C, and different crystallization times. The values in brackets represent the refined lattice parameter *a*.

[Color figure can be viewed at wileyonlinelibrary.com]

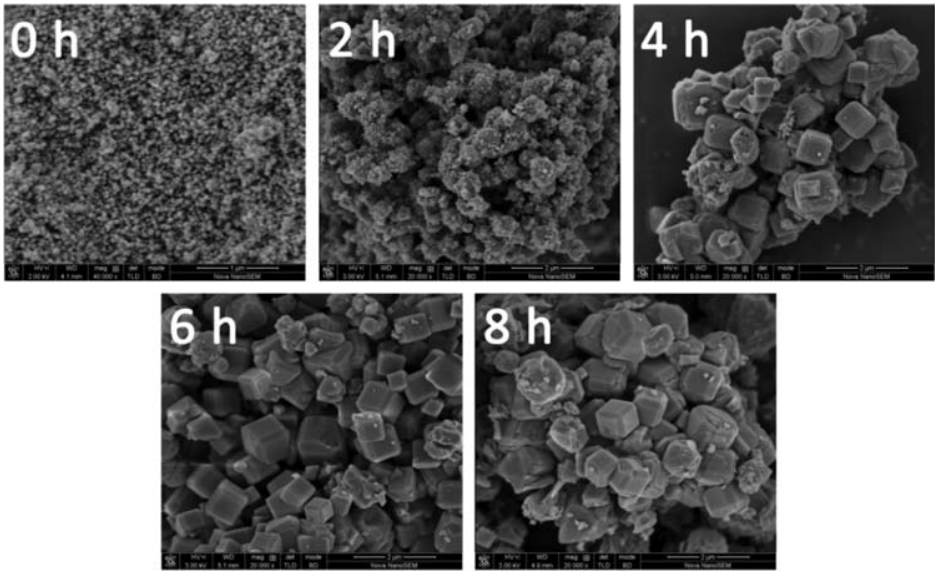

Figure 4. SEM images of synthesized samples using NaOH concentration of 1.6 mol/L, crystallization temperature of 80°C, and different crystallization times.

growth but also largely affect the release of Si species from silica nanoparticles as well as the diffusion of Al species into spherical silica substrates.

Effect of NaOH concentration

Concentration of NaOH used in crystallization system is another crucial parameter determining the formation of zeolites A. Figure 8 displays the XRD patterns of the samples synthesized under different NaOH concentrations. With the concentrations increasing from 0.8 to 1.6 mol/L, the samples have a completely unique zeolite A phase and the continuously increasing crystallinity (see Table 2). It can be supported by the SEM measurements by presenting the reduced number of silica nanoparticles in the aggregates. However, both the XRD patterns (see Figure 8) and SEM images (see Figure 9) for the samples with respect to NaOH concentrations of 2.0 and 2.4 mol/L show the formation of SOD in synthesized products, indicating that higher NaOH concentrations (i.e., 2.0 and 2.4 mol/L) can result in the phase transition from LTA to SOD. As a result, the suitable NaOH concentration was considered to be around 1.6 mol/L.

Effect of Al_2O_3/SiO_2 molar ratios in raw materials

The influence of starting Al_2O_3/SiO_2 molar ratios of raw materials on the synthesized binderless zeolite A is presented in Table 3. The results for $Al_2O_3/SiO_2 = 1.0$ can be found in Table 2 (samples S2∼S5). Conventionally, a molar ratio of Al_2O_3/SiO_2 of 0.5 can be used for the hydrothermal synthesis

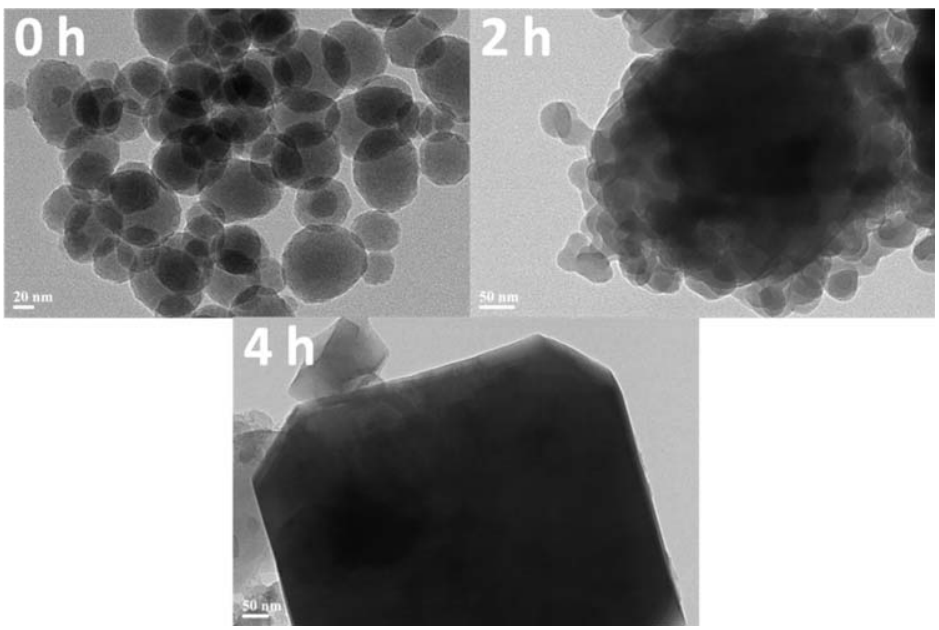

Figure 5. TEM images of synthesized samples using NaOH concentration of 1.6 mol/L, crystallization temperature of 80°C, and different crystallization times.

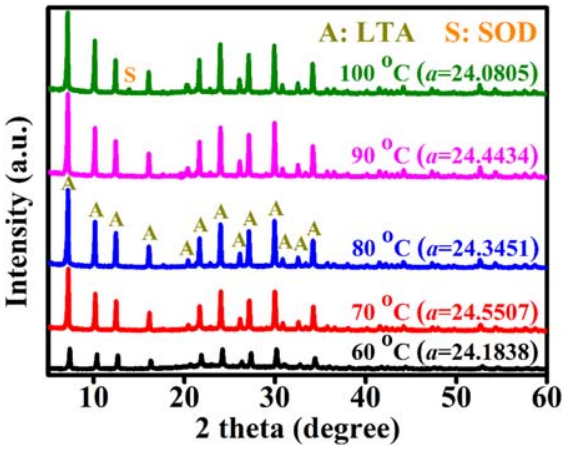

Figure 6. XRD patterns of synthesized samples using NaOH concentration of 1.6 mol/L, crystallization time of 6 h, and different crystallization temperatures. The values in brackets represent the refined lattice parameter *a*.

[Color figure can be viewed at wileyonlinelibrary.com]

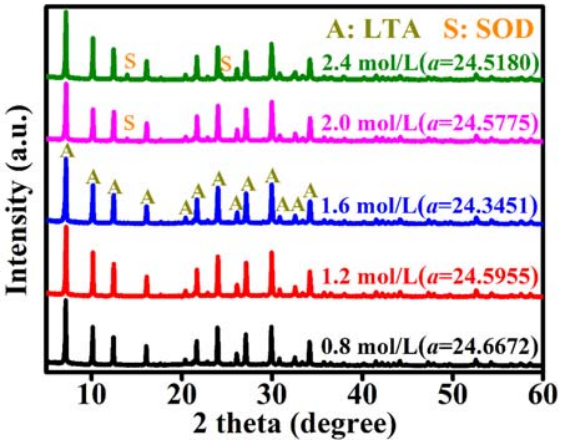

Figure 8. XRD patterns of synthesized samples using crystallization time of 6 h, crystallization temperature of 80°C, and different NaOH concentrations. The values in brackets represent the refined lattice parameter *a*.

[Color figure can be viewed at wileyonlinelibrary.com]

of zeolite A. However, it is not applicable to present in situ synthesis using silica gel precursors because of the quite different contacting scheme between Al and Si species. As shown in Table 3, when Al_2O_3/SiO_2 molar ratios for synthesis systems are 0.5 and 0.75, Al/Si molar ratios of resulting samples finally reach 0.83 and 0.93, respectively, with the increase of crystallization time. In addition to crystallization temperature, the concentration gradient of Al species existing between bulk solution and silica precursors also largely determines the diffusion of Al sources into silica precursors. As a result, it is almost impossible that all of the Al species in solution can diffuse into silica gel precursors to react with silica species at $Al_2O_3/SiO_2 = 0.5$. Larger Al_2O_3/SiO_2 is, therefore, required to achieve a complete conversion of silica gel precursor. As Al_2O_3/SiO_2 molar ratio is increased to 1.0, Al/Si molar ratio of the sample crystallized for 6 h is observed to be 0.96 (sample S4). Consequently, the suitable molar ratio of Al_2O_3/SiO_2 of starting synthesis system was considered to be 1.0.

Crystallization kinetics

In contrast to the conventional hydrothermal synthesis of zeolite A, present in situ conversion shows the significantly different crystallization kinetics. The supply of Al and Si species, which is essential for the growth of zeolite A crystals, is dominated by both the release of Si species from the silica nanoparticles and the diffusion of Al species into silica gel precursors. Consequently, there is the complex dependence of crystallization kinetics for the in situ conversion of silica precursors on reaction temperature, duration, and alkalinity of the hydrothermal system. To track the crystallization process, a

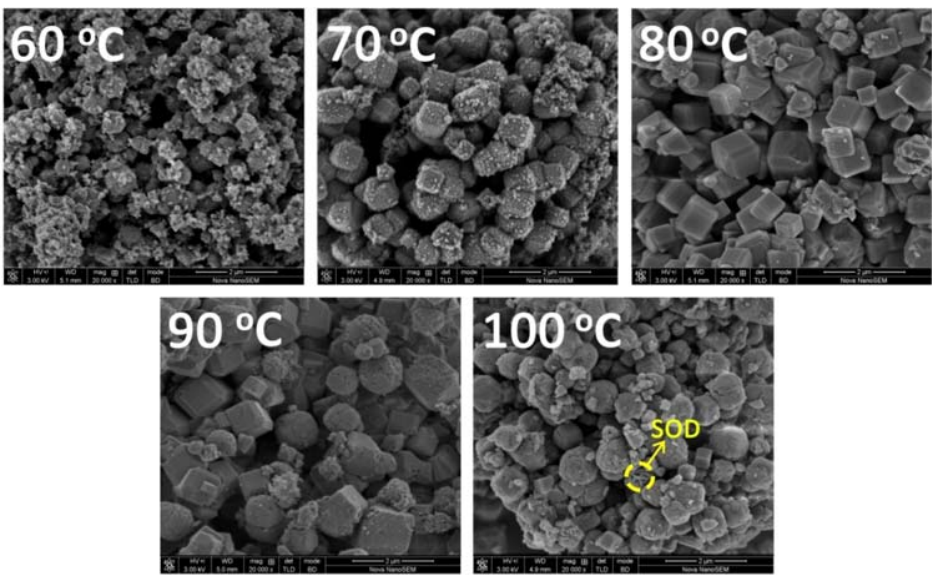

Figure 7. SEM images of synthesized samples using NaOH concentration of 1.6 mol/L, crystallization time of 6 h, and different crystallization temperatures.

[Color figure can be viewed at wileyonlinelibrary.com]

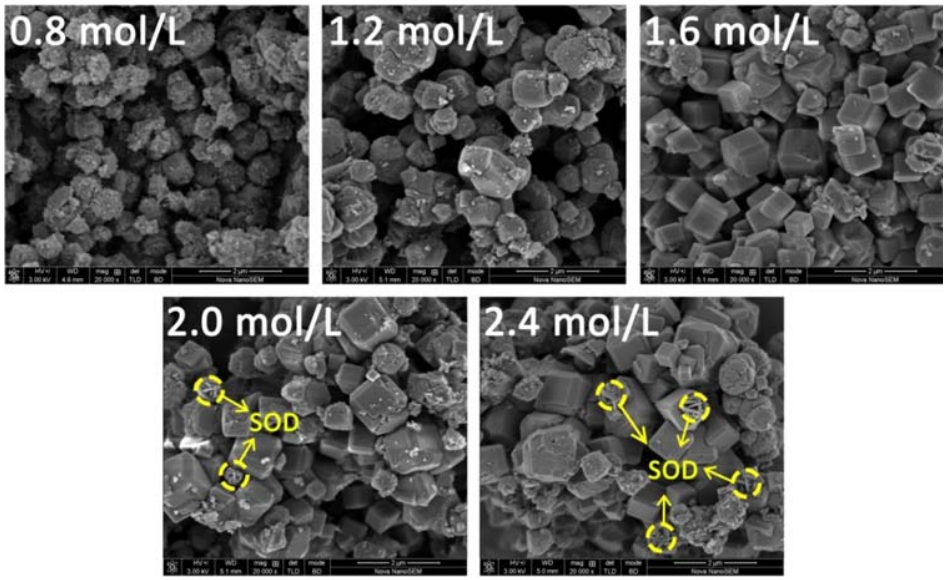

Figure 9. SEM images of synthesized samples using crystallization time of 6 h, crystallization temperature of 80°C, and different NaOH concentrations.

[Color figure can be viewed at wileyonlinelibrary.com]

series of synthesis experiments using different NaOH concentrations were performed at a relatively low reaction temperature of 60°C (see Figure 10 for the crystallization kinetics curves).

Using the Avrami - Erofe'ev (A-E) model,[39–41] the crystallization kinetic curves could be well explained. The relative crystallinity, γ, is a function of crystallization time and can be described as Eq. 1

$$\gamma=[1-\exp(-(k(t-\theta))^n)]\times 100\% \quad (1)$$

where t and θ are the crystallization time and induction time, respectively. k is the apparent rate constant of crystallization. And n is the Avrami exponent, a parameter concerning the mechanism for nucleation as well as crystal growth.

Then the crystallization curves were correlated using A-E model and the Avrami exponent n and rate constant k could be derived (see Supporting Information Table S2). The fitting results are also shown in Figure 10 (solid lines). Avrami exponent n is determined by both the dimensionality of crystal growth space and the rate-determining growth mechanism.[42] As shown in Supporting Information Table S2, n increases from 1.50 to 6.25 with NaOH concentration rising from 0.4 to 2.0 mol/L. The continuously increasing n value suggests that the crystallization process can be largely affected by the dissolution rate of silica nanoparticles and the diffusion of Al species into silica gel precursors. Present results confirm that the growth of crystals can be accelerated by reasonably increasing NaOH concentration. Once the concentration gets increased, the dissolution rate of silica nanoparticles into the alkaline microenvironment will be enhanced largely. However, the crystal growth is susceptible to the diffusion rate of Al species that is approximately invariable under the fixed temperature (60°C). Consequently, the Al species are insufficient for crystal growth at higher NaOH concentration because of their limited rate of diffusion into silica precursors, which is considered to be the remarkable distinction between traditional hydrothermal synthesis and present in-situ conversion originated from silica matrix. An increased apparent rate constant, k, further confirms that the increment of NaOH concentration is beneficial to the growth of zeolite crystals.

Crystallization mechanism

To reveal the underlying mechanism for the in situ formation of zeolite LTA originated from silica gel precursors, samples were collected at various crystallization times and characterized using Raman as well as ^{29}Si and ^{27}Al MAS NMR analyses (see Figure 11). NaOH concentration and crystallization temperature were fixed at 1.6 mol/L and 60°C, respectively. In the case of 4 h, the Raman spectrum exhibits a weak peak at 501 cm^{-1} assigned to four-membered rings

Table 3. Chemical Compositions (on TO_2 Basis) of Synthesized Samples Using Crystallization Temperature of 80°C, NaOH Concentration of 1.6 mol/L, and Different Al_2O_3/SiO_2 Molar Ratios

Sample No.	Used Al_2O_3/SiO_2 for Synthesis	Crystallization Time [h]	Chemical Composition of Synthesized Samples	Al/Si of Samples
S14	0.5	2	$Na_{0.387}Al_{0.387}Si_{0.613}O_2$	0.63
S15		4	$Na_{0.438}Al_{0.438}Si_{0.562}O_2$	0.78
S16		6	$Na_{0.450}Al_{0.450}Si_{0.550}O_2$	0.82
S17		8	$Na_{0.454}Al_{0.454}Si_{0.546}O_2$	0.83
S18	0.75	2	$Na_{0.394}Al_{0.394}Si_{0.606}O_2$	0.65
S19		4	$Na_{0.451}Al_{0.451}Si_{0.549}O_2$	0.82
S20		6	$Na_{0.459}Al_{0.459}Si_{0.541}O_2$	0.85
S21		8	$Na_{0.482}Al_{0.482}Si_{0.518}O_2$	0.93

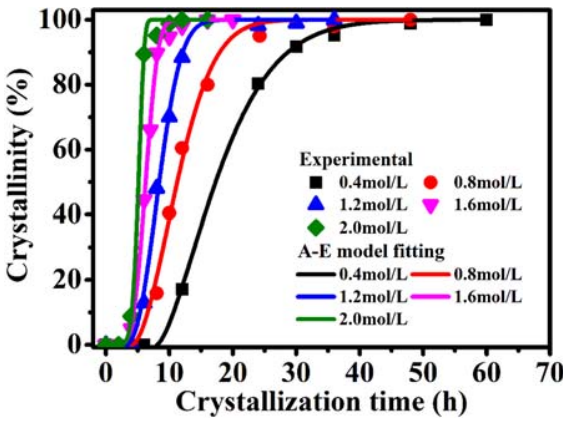

Figure 10. Crystallization kinetics curves for the in situ synthesis of zeolite A on silica precursors at crystallization temperature of 60°C and different NaOH concentrations.

[Color figure can be viewed at wileyonlinelibrary.com]

(4R),[43] indicating the initial formation of primary structure units of LTA framework. The ^{29}Si MAS NMR spectrum for this sample presents the chemical shift at −100∼–120 ppm, mainly associated with the SiO_2 (resulting from the original silica precursors) and Si-(O-Al)- (Si linking to only one Al atom through the oxygen bridge) species. And the ^{27}Al MAS NMR spectrum demonstrates a wide chemical shift ranging from 50 to 80 ppm concerning the multiple chemical circumstances that the Al species immerse into (binding to different number of -O-Si- groups). As crystallization time reaches 6 h, the Raman signal of 4R species becomes stronger. Meanwhile, two new bands appear at 301 and 361 cm^{-1}, respectively, corresponding to eight-membered rings (8R) and six-membered rings (6R).[44] Additionally, the ^{29}Si MAS NMR spectrum displays a chemical shift at $\delta = -86.8$ ppm (see Figure 11B) that is mainly attributed to Si species of Si-(O-Al)$_4$- groups with respect to the 6 h sample (having relative crystallinity of 42.5%).[45,46] After 8 h of crystallization, a remarkable peak shift from 501 to 509 cm^{-1} takes place, corresponding to a characteristic vibration band of 4R in LTA framework. From its ^{29}Si MAS NMR spectrum, the chemical shift at around −110 ppm is largely vanished due to the transformation of Si species from silica nanoparticles into structural units of LTA framework. Continuing to increase the crystallization time up to 12 h, all Raman peaks retain at the same positions while the intensities of these peaks become stronger as expected. In 8 and 12 h cases, the ^{29}Si and ^{27}Al MAS NMR spectra exhibit the single sharp peak at −87.6 and 60 ppm, respectively, corresponding to the structural Si and Al species of the LTA frameworks. It is shown that the ordered LTA frameworks are formed along with the consumption of reactants of Si and Al species (see Figures 3–5 for the XRD patterns, SEM, and TEM images, respectively).

Present results confirm that the silica gel precursors are converted into binderless zeolite spheres based on the following in situ synthesis mechanism: Al sources in solution gradually diffuse into spherical silica gel precursors while the silica nanoparticles contained in precursors start to dissolve to provide silica species for the nucleation (see Figure 5). These Al species then can link with dissolved Si species by means of oxygen bridges to form the primary building units (BU). Finally, they construct the second building units (SBU) via self-assembling and create the complete LTA framework through self-organized arrangement of building units. The formation of LTA framework is involved in an in situ conversion process occurring at the silica precursors (see Figure 12).

In summary, the crystallization mechanism with respect to the synthesis of binderless zeolite A pellets via in situ hydrothermal conversion is in accordance with what is proposed by Rimer et al.[47] for synthesizing zeolite LTA powder using silica sol as Si source. However, there are still differences between these two synthesis processes. In the Rimer's synthesis system, silica nanoparticles could more easily contact with Al sources. As for present in situ transformation process using preformed silica gel precursors, Al sources dissolved in solution need to diffuse into granular silica gel precursors which consist of a large number of silica nanoparticles. Due to the significant diffusion resistance, the influences of synthesis conditions (i.e., crystallization temperature and NaOH

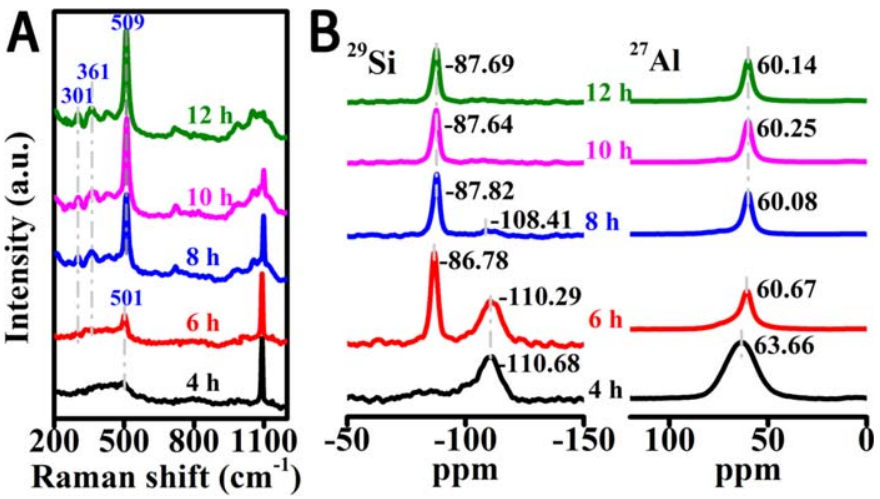

Figure 11. UV-Raman spectra (A) and ^{29}Si and ^{27}Al MAS NMR spectra (B) of the samples synthesized at different crystallization times using NaOH concentration of 1.6 mol/L and crystallization temperature of 60°C, respectively.

[Color figure can be viewed at wileyonlinelibrary.com]

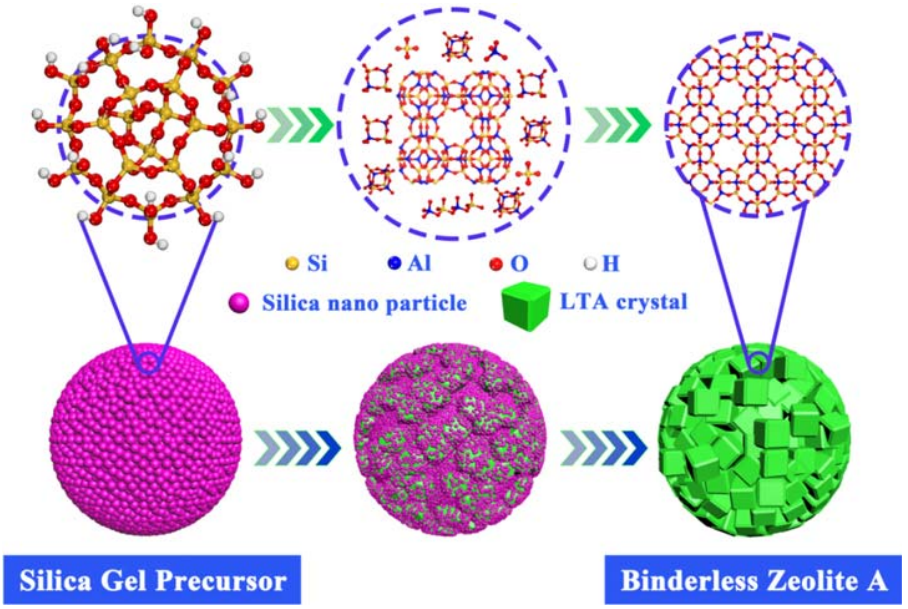

Figure 12. Crystallization route for the in situ synthesis of binderless zeolite A on silica gel precursors.

[Color figure can be viewed at wileyonlinelibrary.com]

concentration) on nucleation rate, therefore, become much greater than conventional hydrothermal synthesis concerning silica nanoparticles or Si sources dissolved in synthesis solution. Furthermore, the diffusion of Al species into silica gel precursors largely determines the nucleation and growth rate.

Adsorption performance of synthesized binderless 5A

N_2 adsorption-desorption isotherms and pore structure analysis results for the synthesized binderless 5A, commercial binderless 5A, and the binder-containing reference sample are presented in Supporting Information Figure S2 and Table 4, respectively. As compared to the zeolite with binder, the synthesized binderless LTA sample shows 28% higher specific surface area (640 vs. 498 m^2/g). The mass fraction of binder in binder-containing reference sample was evaluated to be 19.2% according to XRD characterizations (see Supporting Information Figure S1). On a basis of pure zeolite A phase, the binder-containing sample still exhibits smaller specific surface area than the synthesized binderless sample (616 vs. 640 m^2/g). Moreover, both binderless zeolite samples display larger macropore diameters (see Table 4 and Supporting Information Figure S3) as compared with the binder-containing sample. It can be easily explained that the binder species in binder-containing sample can fill the space among zeolite crystals (macropore) and leave smaller pore (mesopore) (see Supporting Information Figure S4). In comparison, the binderless zeolite samples have much more macropore, which superior secondary pore system can facilitate faster diffusion of molecules. Present results are in good agreement with previous studies on the pore structure and diffusion involving binderless zeolite X- and A-type zeolites.[16,48]

To evaluate the adsorption capacity of n-paraffins on synthesized binderless zeolite 5A samples, adsorption isotherms of several n-paraffins were measured and compared with the binder-containing commercial product. Figure 13 presents the adsorption isotherms of n-paraffins on two samples at 298 K. n-C_5~n-C_8 paraffins show higher adsorption capacities on synthesized binderless sample than the referenced binder-containing zeolite. Furthermore, the experimental adsorption isotherms were correlated using various thermodynamic models. In comparison with the theoretical Langmuir model and the empirical Freundlich model, the semiempirical Langmuir-Freundlich (L–F) model could explain the experimental isotherm data very well. This model supposes that the adsorption process involves heterogeneous as well as homogeneous adsorption simultaneously. It can be expressed as Eq. 2

$$q_e = q_{\max} \frac{(bP_e)^N}{1+(bP_e)^N} \tag{2}$$

where b and N are the L–F constants, respectively. $q_{\max}$ is the maximum adsorption capacity. And q_e refers to adsorption amount (mg/g-zeolite) under the equilibrium pressure of P_e (Pa).

In addition, a dimensionless constant that is defined as the separation factor (R_L) was used to evaluate the relative adsorption performance of various adsorbates on different porous materials and could be calculated using Eq. 3. R_L value

Table 4. Pore Structure Analysis Results of Different Zeolite 5A Samples

		Micropore		Mesopore		Macropore	
Samples	S_{BET} [m^2/g]	Diameter [nm]	Volume [cm^3/g]	Diameter [nm]	Volume [cm^3/g]	Diameter [nm]	Volume [cm^3/g]
Synthesized binderless zeolite	640	0.59	0.24	7.65	0.069	320.5	0.21
Commercial binderless zeolite	596	0.62	0.24	5.25	0.075	425.3	0.22
Binder-containing zeolite	498	0.58	0.19	9.88	0.10	156.5	0.24

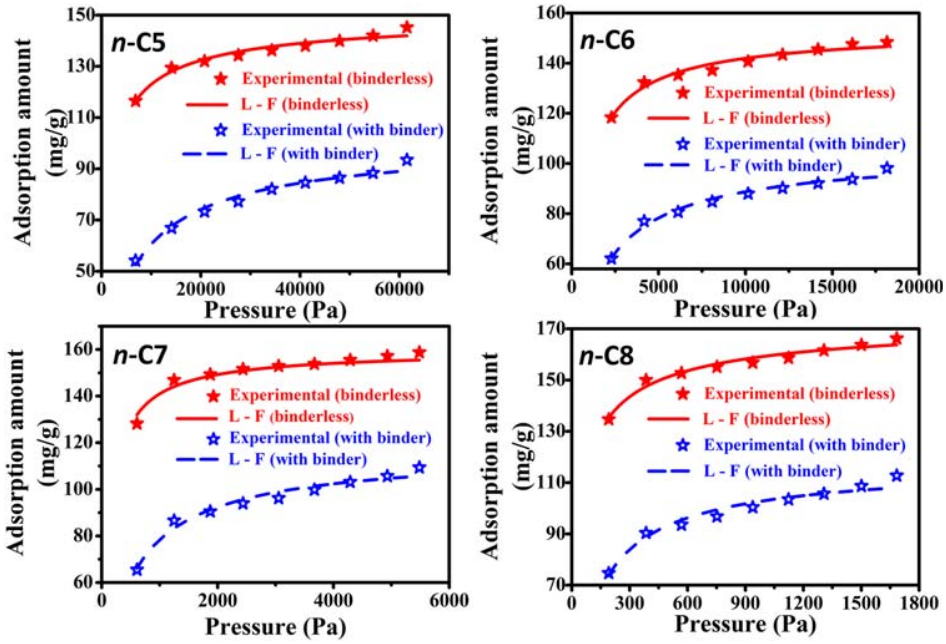

Figure 13. Isotherms for n-paraffins adsorption on the synthesized binderless zeolite sample and the binder-containing sample at 298 K (points: experimental values, lines: fitting results from L-F model).

[Color figure can be viewed at wileyonlinelibrary.com]

represents the nature of adsorption: unfavorable ($R_L > 1$), linear ($R_L = 1$), favorable ($0 < R_L < 1$) or irreversible ($R_L = 0$).[49] Lower R_L value indicates the more favorable adsorption

$$R_L = \frac{1}{1 + bP_0} \tag{3}$$

where, P_0 represents the initial pressure of adsorbate in adsorption system (Pa).

The adsorption equilibrium data fitted by applying L–F model are also presented in Figure 13 and the fitting parameters are listed in Supporting Information Table S3. The synthesized binderless zeolite LTA spheres have around 36–49% higher q_{max} than the binder-containing pellets, agreeing well with our experimental results. Our early investigation has indicated that the influence of binder on adsorption capacity of pelletized zeolite could be attributed to the dilution and aperture blocking effects of binder species on zeolite crystals.[13] Present results are in accordance with previous conclusion. On one hand, zeolite A phase in sample can be diluted by the addition of binder that does not contribute to the adsorption. On the other hand, the binder, which attaches to the surface of zeolite crystals (see Supporting Information Figure S4), blocks the pores and channels resulting in a suppression of adsorption ability and increase in diffusion resistance. Therefore, the synthesized binderless sample still exhibits around 17% higher adsorption capacity when the comparison is based on pure zeolite A phase of the two samples (see Supporting Information Table S3).

Table 5. Mechanical Strength of Different Zeolite 5A Samples

Samples	Mechanical Strength [N]
Synthesized binderless zeolite 5A	41 ± 2
Commercial binderless zeolite 5A	39 ± 2
Binder-containing zeolite 5A	72 ± 3

It is worthy to note that the binderless zeolite has higher adsorption affinity to adsorbate molecules (smaller R_L) than the reference binder-containing sample. An increase in adsorption selectivity can be attributed to the elimination of influence of binder on pore structure of zeolite sample. As a result, the synthesized binderless zeolite A will exhibit great superiority of adsorption capacity, diffusion rate and selectivity of normal paraffins over the binder-containing products, and can be expected to contribute to the higher performance and more economical separation of normal paraffins from complex hydrocarbon mixtures.

Mechanical properties and hydrothermal stability of synthesized binderless 5A

Mechanical strength of different zeolite 5A samples was measured and the results are shown in Table 5. The synthesized binderless sample shows mechanical strength of 41 N which is very close to that of commercial binderless sample. From the measurement results, the synthesized binderless sample has satisfactory mechanical property for industrial applications. The better strength of binder-containing sample is attributed to adding of binder which can fill the space among zeolite crystals and help cement the crystals together tightly (see Supporting Information Figure S4).

In addition, the hydrothermal stability of different zeolite samples was examined by employing a facile hydrothermal treatment in boiling water for 24 h. The static adsorption capacities for three samples treated under hydrothermal condition were compared with the fresh parent samples. The reserved adsorption ability (%) was used to evaluate their hydrothermal stability. The static adsorption capacity of each sample was determined by measuring the concentration change of n-hexane in a hexane–cyclohexane–zeolite system at 25°C using initial n-hexane concentration of around 5% in weight. As expected, three samples show less than 3% decrease of adsorption capacity after hydrothermal treatment

(see Supporting Information Figure S5), indicating that the synthesized binderless sample has comparative hydrothermal stability to the commercial binder-containing sample.

Conclusions

We demonstrate a one-pot synthesis route for the preparation of binderless zeolite A via an in situ hydrothermal transformation process concerning preformed silica gel precursors. The influences of crystallization time, temperature and NaOH concentration on conversion of silica precursors were examined. The synthesized samples were characterized in terms of multitechnique method. In addition, the crystallization kinetics and mechanism for the in situ synthesis of zeolite A on silica matrix were explored. Present results indicate that both crystallization temperature and NaOH concentration play the crucial roles in controlling the in situ transformation process via governing the dissolution rates of silica nanoparticles, the diffusion of Al species into silica precursors and crystal nuclei growth. Al species can diffuse into silica precursors and react with released Si species from silica nanoparticles to form the structural building units and finally generate the LTA framework through self-organized arrangement of building units. The synthesized binder-free sample is confirmed to exhibit great superiority of adsorption capability of normal paraffins over the binder-containing sample, providing a potential alternative for binder-containing zeolites in the industrial applications in adsorption and separation to improve their efficiency.

Acknowledgments

This work is financially supported by the Training Program of the Major Research Plan of the National Natural Science Foundation of China (Grant 91634112), the Natural Science Foundation of Shanghai (Grant 16ZR1408100) and the Open Project of State Key Laboratory of Chemical Engineering (SKL-ChE-16C01). D.W. acknowledges the institutional funds from the Gene and Linda Voiland School of Chemical Engineering and Bioengineering at Washington State University.

Literature Cited

1. Weitkamp J, Puppe L. *Catalysis and Zeolites: Fundamentals and Applications*. Heidelberg: Springer, 1999.
2. Auerbach SM, Carrado KA, Dutta PK. *Handbook of Zeolite Science and Technology*. London: Taylor & Francis, 2003.
3. Song J, Liu M, Zhang Y. Ion-exchange adsorption of calcium ions from water and geothermal water with modified zeolite A. *AIChE J*. 2015;61(2):640–654.
4. Corma A. Inorganic solid acids and their use in acid-catalyzed hydrocarbon reactions. *Chem Rev*. 1995;95(3):559–614.
5. Chen NY, Garwood WE, Dwyer FG. *Shape Selective Catalysis in Industrial Applications*, 2nd ed. New York: Macel Dekker, Inc., 1996.
6. Yang P, Ye X, Lau C, Li Z, Liu X, Lu J. Design of efficient zeolite sensor materials for n-hexane. *Anal Chem*. 2007;79:1425–1432.
7. Sivasankar N, Vasudevan S. Adsorption of n-hexane in zeolite-5A: a temperature-programmed desorption and IR-spectroscopic study. *J Phys Chem B*. 2005;109(32):15417–15421.
8. Chen L, Wang YW, He MY, Chen Q, Zhang ZH. Facile synthesis of 5A zeolite from attapulgite clay for adsorption of n-paraffins. *Adsorption*. 2016;22(3):309–314.
9. Barrer RM. *Hydrothermal Chemistry of Zeolites*. London: Academic Press, 1982.
10. Cundy CS, Cox PA. The hydrothermal synthesis of zeolites: history and development from the earliest days to the present time. *Chem Rev*. 2003;103(3):663–701.
11. Breck DW. *Zeolite Molecular Sieves: Structure, Chemistry and Use*. New York: John Wiley & Sons, 1974.
12. Silva JAC, Rodrigues AE. Equilibrium and kinetics of n-hexane sorption in pellets of 5A zeolite. *AIChE J*. 1997;43(10):2524–2534.
13. Sun H, Shen B, Liu J. N-Paraffins adsorption with 5A zeolites: the effect of binder on adsorption equilibria. *Sep Purif Technol*. 2008; 64(1):135–139.
14. Shams K, Mirmohammadi SJ. Preparation of 5A zeolite monolith granular extrudates using kaolin: investigation of the effect of binder on sieving/adsorption properties using a mixture of linear and branched paraffin hydrocarbons. *Microporous Mesoporous Mater*. 2007;106(1–3):268–277.
15. Charkhi A, Kazemeini M, Ahmadi SJ, Kazemian H. Fabrication of granulated NaY zeolite nanoparticles using a new method and study the adsorption properties. *Powder Technol*. 2012;231:1–6.
16. Mehlhorn D, Valiullin R, Kärger J, Schumann K, Brandt A, Unger B. Transport enhancement in binderless zeolite X- and A-type molecular sieves revealed by PFG NMR diffusometry. *Microporous Mesoporous Mater*. 2014;188:126–132.
17. Sun H, Shen B. Experimental study on coking, deactivation, and regeneration of binderless 5A zeolite during 1-hexene adsorption. *Adsorption*. 2013;19(1):111–120.
18. Silva JAC, Mata VG, Dias MM, Lopes JCB, Rodrigues AE. Effect of coke in the equilibrium and kinetics of sorption on 5A molecular sieve zeolites. *Ind Eng Chem Res*. 2000;39(4):1030–1034.
19. Hargreaves JSJ, Munnoch AL. A survey of the influence of binders in zeolite catalysis. *Catal Sci Technol*. 2013;3(5):1165–1171.
20. De Lucas A, Valverde JL, Sánchez P, Dorado F, Ramos MJ. Influence of the binder on the n-octane hydroisomerization over palladium-containing zeolite catalysts. *Ind Eng Chem Res*. 2004; 43(26):8217–8225.
21. Universal Oil Products Company. Method for preparing high rate zeolitic molecular sieve particles. U.S. Patent No. 3 348 911; 1967.
22. Universal Oil Products Company. Preparation of crystalline zeolite particles. U.S. Patent No. 3 359 068; 1967.
23. Li SA, Ke YZ, Tang C, Zhao EY. Preparation of binderless zeolite A granules. CN. Patent No. 87 105 499 A; 1988.
24. Vasiliev P, Akhtar F, Grins J, Mouzon J, Andersson C, Hedlund J, Bergström L. Strong hierarchically porous monoliths by pulsed current processing of zeolite powder assemblies. *ACS Appl Mater Inter*. 2010;2(3):732–737.
25. Prokof'ev VY, Gordina NE, Khramtsova AP, Konstantinova EM, Cherednikova DS. Synthesis of binder-free granulated low-modular zeolites using ultrasound. *Microporous Mesoporous Mater*. 2017;242:63–73.
26. Li WC, Lu AH, Palkovits R, Schmidt W, Spliethoff B, Schüth F. Hierarchically structured monolithic silicalite-1 consisting of crystallized nanoparticles and its performance in the Beckmann rearrangement of cyclohexanone oxime. *J Am Chem Soc*. 2005;127:12595–12600.
27. Özcan A, Kalıpçılar H. Preparation of zeolite A tubes from amorphous aluminosilicate extrudates. *Ind Eng Chem Res*. 2006;45:4977–4984.
28. Zhang L, Yao J, Zeng C, Xu N. Combinatorial synthesis of SAPO-34 via vapor-phase transport. *Chem Commun*. 2003;(17):2232–2233.
29. Ren L, Wu Q, Yang C, Zhu L, Li C, Zhang P, Zhang H, Meng X, Xiao FS. Solvent-free synthesis of zeolites from solid raw materials. *J Am Chem Soc*. 2012;134(37):15173–15176.
30. Jin Y, Sun Q, Qi G, Yang C, Xu J, Chen F, Meng X, Deng F, Xiao FS. Solvent-free synthesis of silicoaluminophosphate zeolites. *Angew Chem*. 2013;125(35):9342–9345.
31. Universal Oil Products Company. Process for preparing molecular sieve bodies. U.S. Patent No. 4 818 508; 1989.
32. Shimizu S, Hamada H. Direct conversion of bulk materials into MFI zeolites by a bulk-material dissolution technique. *Adv Mater*. 2000; 12(18):1332–1335.
33. Martin T, Galarneau A, Renzo FD, Fajula F, Plee D. Morphological control of MCM-41 by pseudomorphic synthesis. *Angew Chem Int Ed*. 2002;41(14):2590–2592.
34. Yu L, Gong J, Zeng C, Zhang L. Synthesis of monodisperse zeolite A/chitosan hybrid microspheres and binderless zeolite A microspheres. *Ind Eng Chem Res*. 2012;51(5):2299–2308.
35. Yan B, Zeng C, Yu L, Wang C, Zhang L. Preparation of hollow zeolite NaA/chitosan composite microspheres via in situ hydrolysis–gelation− hydrothermal synthesis of TEOS. *Microporous Mesoporous Mater*. 2018;257:262–271.
36. Anuwattana R, Khummongkol P. Conventional hydrothermal synthesis of Na-A zeolite from cupola slag and aluminum sludge. *J Hazard Mater*. 2009;166(1):227–232.
37. Grämlich V, Meier WM. The crystal structure of hydrated NaA: A detailed refinement of a pseudosymmetric zeolite structure. *Z Kristallogr*. 1971;133(133):134–149.

38. Qian T, Li J. Synthesis of Na-A zeolite from coal gangue with the in-situ crystallization technique. *Adv Powder Technol*. 2015;26(1): 98–104.
39. Zhang RH, Li XK, Cao GP, Shi YH, Liu HL, Yuan WK, Roberts GW. Improved kinetic model of crystallization for isotactic polypropylene induced by supercritical CO_2: introducing pressure and temperature dependence into the Avrami equation. *Ind Eng Chem. Res*. 2011;50(18):10509–10515.
40. Finney EE, Finke RG. Is there a minimal chemical mechanism underlying classical Avrami-Erofe'ev treatments of phase-transformation kinetic data? *Chem Mater*. 2009;21(19):4692–4705.
41. Finney EE, Shields SP, Buhro WE, Finke RG. Gold nanocluster agglomeration kinetic studies: evidence for parallel bimolecular plus autocatalytic agglomeration pathways as a mechanism-based alternative to an Avrami-based analysis. *Chem Mater*. 2012;24(10):1718–1725.
42. Miladinović ZP, Zakrzewska J, Kovačević BT, Miladinović JM. In situ ^{27}Al NMR kinetic investigation of zeolite A crystallization. *Microporous Mesoporous Mater*. 2014;195:131–142.
43. Ren L, Li C, Fan F, Guo Q, Liang D, Feng Z, Li C, Li S, Xiao FS. UV–Raman and NMR spectroscopic studies on the crystallization of zeolite A and a new synthetic route. *Chem Eur J*. 2011;17(22):6162–6169.
44. Yu Y, Xiong G, Li C, Xiao FS. Characterization of aluminosilicate zeolites by UV Raman spectroscopy. *Microporous Mesoporous Mater*. 2001;46(1):23–34.
45. Su S, Ma H, Chuan X. Hydrothermal synthesis of zeolite A from K-feldspar and its crystallization mechanism. *Adv Powder Technol*. 2016;27(1):139–144.
46. Xiao Y, Sheng N, Chu Y, Wang Y, Wu Q, Liu X, Deng F, Meng X, Feng Z. Mechanism on solvent-free crystallization of NaA zeolite. *Microporous Mesoporous Mater*. 2017;237:201–209.
47. Oleksiak MD, Soltis JA, Conato MT, Penn RL, Rimer JD. Nucleation of FAU and LTA zeolites from heterogeneous aluminosilicate precursors. *Chem Mater*. 2016;28(14):4906–4916.
48. Schumann K, Unger B, Brandt A, Scheffler F. Investigation on the pore structure of binderless zeolite 13X shapes. *Microporous Mesoporous Mater*. 2012;154:119–123.
49. Weber TW, Chakravorti RK. Pore and solid diffusion models for fixed-bed adsorbers. *AIChE J*. 1974;20(2):228–238.

Manuscript received Apr. 3, 2018